

# Angle-Resolved Raman Imaging of Interlayer Rotations and Interactions in Twisted Bilayer Graphene

Robin W. Havener,<sup>†</sup> Houlong Zhuang,<sup>‡</sup> Lola Brown,<sup>§</sup> Richard G. Hennig,<sup>‡</sup> and Jiwoong Park<sup>\*,§,⊥</sup>

<sup>†</sup>School of Applied and Engineering Physics, Cornell University, Ithaca, New York 14853, United States

<sup>‡</sup>Department of Materials Science and Engineering, Cornell University, Ithaca, New York 14853, United States

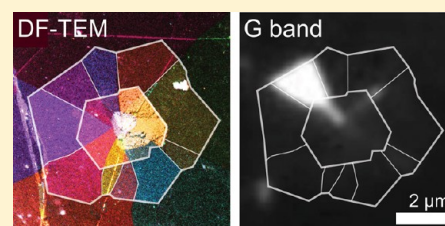
<sup>§</sup>Department of Chemistry and Chemical Biology, Cornell University, Ithaca, New York 14853, United States

<sup>⊥</sup>Kavli Institute at Cornell for Nanoscale Science, Cornell University, Ithaca, New York 14853, United States

## S Supporting Information

**ABSTRACT:** Few-layer graphene is a prototypical layered material, whose properties are determined by the relative orientations and interactions between layers. Exciting electrical and optical phenomena have been observed for the special case of Bernal-stacked few-layer graphene, but structure–property correlations in graphene which deviates from this structure are not well understood. Here, we combine two direct imaging techniques, dark-field transmission electron microscopy (DF-TEM) and widefield Raman imaging, to establish a robust, one-to-one correlation between twist angle and Raman intensity in twisted bilayer graphene (tBLG). The Raman G band intensity is strongly enhanced due to a previously unreported singularity in the joint density of states of tBLG, whose energy is exclusively a function of twist angle and whose optical transition strength is governed by interlayer interactions, enabling direct optical imaging of these parameters. Furthermore, our findings suggest future potential for novel optical and optoelectronic tBLG devices with angle-dependent, tunable characteristics.

**KEYWORDS:** Graphene, twisted bilayer, Raman spectroscopy, dark-field TEM, imaging



Bilayer graphene produced by mechanical exfoliation of HOPG is almost exclusively Bernal-stacked and possesses properties distinct from those of single-layer graphene,<sup>1,2</sup> such as the opening of a band gap under a perpendicular electric field<sup>3,4</sup> and unique Raman<sup>5–7</sup> and infrared<sup>8,9</sup> optical spectra. However, many departures from this structure are possible for a multilayer system, including variations in interlayer distance, strain, stacking faults, and rotational mismatches,<sup>10,11</sup> resulting in new electronic, optical, and mechanical behaviors.<sup>12–17</sup> In particular, recent experiments have shown that a significant proportion of the bilayer graphene produced by chemical vapor deposition (CVD) is twisted bilayer graphene (tBLG),<sup>10,18</sup> where the layers are rotated by a relative angle  $\theta$  (Figure 1a, inset).

Recent scanning tunneling spectroscopy,<sup>19,20</sup> Raman spectroscopy,<sup>21–25</sup> and optical absorption<sup>26</sup> studies of tBLG have provided evidence of intriguing,  $\theta$ -dependent electronic and optical properties, such as new Van Hove singularities in the low-energy electronic density of states<sup>19</sup> and strong Raman G band enhancement<sup>21,23</sup> at specific angles. However, these studies are not comprehensive enough to generalize the properties of tBLG for arbitrary  $\theta$  because they lack the capability to determine  $\theta$  both accurately and over a large area for many samples. Instead, ideal experiments would allow simultaneous structural identification and studies of physical properties in tBLG with high spatial resolution and high

throughput; such capabilities are essential for understanding structure–property correlations in tBLG.

Indeed, large-scale Raman imaging of CVD tBLG shows distinct, domain-like features not seen in SLG. Figure 1a shows a white light, contrast-enhanced reflection image of CVD graphene transferred to a Si/285 nm SiO<sub>2</sub> substrate, which contains several multilayer areas. The bilayer graphene (BLG) appears darker than single layer graphene (SLG),<sup>27</sup> but with spatially homogeneous intensity. In contrast, a widefield Raman image<sup>28</sup> of the same area shows striking variations in G band intensity within these multilayer areas, with polygonal domains which evoke the orientation angle-dependent grain structure observed in recent DF-TEM studies of CVD graphene.<sup>29,30</sup>

To correlate features like those in Figure 1a with the structure of tBLG, we have developed an imaging platform that allows both Raman and DF-TEM imaging on the same samples. Our CVD graphene is transferred to thin (5 or 10 nm) silicon nitride membranes, which are compatible with both techniques.<sup>28,29</sup> With this, we have imaged over 50 CVD tBLG domains with known twist angles, the data from which are shown in Figures 1b and 2 (and Figures S1, S5, S6, S8, and S9). A representative DF-TEM image, and widefield G and 2D band images ( $E_{\text{ex}} = 2.33$  eV or  $\lambda = 532$  nm), of one area containing

**Received:** March 23, 2012

**Revised:** May 14, 2012

**Published:** May 21, 2012

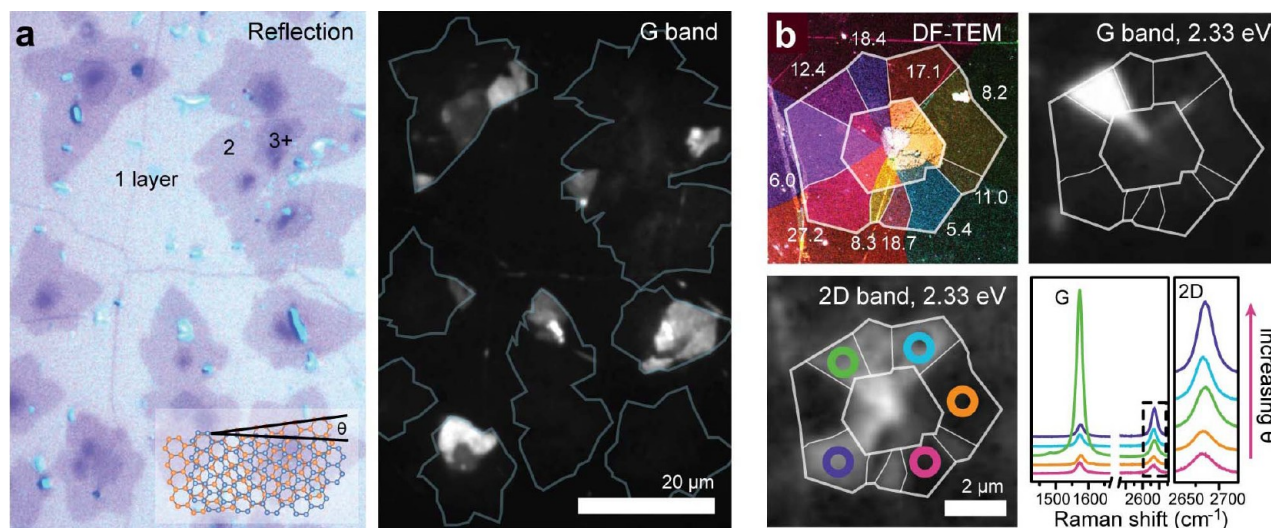


**Figure 1.** (a) An optical reflection image of CVD graphene transferred to Si/285 nm SiO<sub>2</sub> and a large area widefield G band Raman image of the same region. The G band image contains striking features in the multilayer regions, which are not seen in the reflection image. (inset) Structure of tBLG with a twist angle  $\theta$ . (b) Dark-field TEM, G band, and 2D band Raman images of the same multilayer tBLG sample. The features in the Raman image correspond well with twisted bilayer domains identified with DF-TEM ( $\theta$  is labeled for each domain in the TEM image). Raman spectra for several domains are also shown.

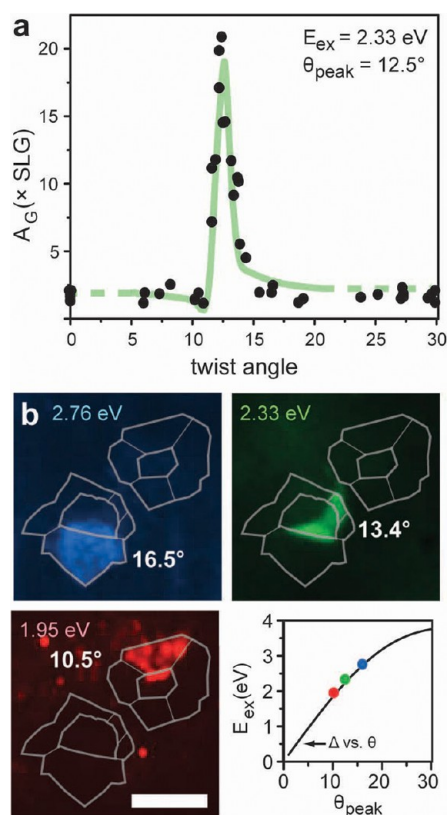


**Figure 2.** (a) A plot of G band integrated intensity ( $A_G$ ) vs  $\theta$  across many tBLG samples. Our data form a universal curve with strong enhancement near one specific twist angle. The fit is from a simplified calculation of G band intensity using our parallel band model, as described in the text and Supporting Information. (b) widefield G band images of the same tBLG regions at three different excitation wavelengths. A different domain exhibits strong G band enhancement in each image (scale bar 5  $\mu\text{m}$ ). Plotted are  $E_{\text{ex}}$  vs  $\theta_{\text{peak}}$  for each of our available excitation wavelengths, based on data from many samples, alongside a plot of the parallel band singularity energy vs  $\theta$  (described in the text).

10 different tBLG domains with varying  $\theta$  is shown in Figure 1b. The DF-TEM image is a false color composite of the domains mapped individually by diffraction-filtered imaging, as in ref 29, while the widefield Raman images were acquired in 2 min apiece using optical bandpass filters, as in ref 28. These images clearly demonstrate that the variations in Raman intensity are strongly correlated with  $\theta$ ; furthermore, the intensity of both bands is nearly constant within a domain. The Raman intensities are also uniform across different tBLG domains with similar  $\theta$  grown under different synthesis parameters (see Supporting Information).

In particular, there is a strong enhancement of the G band integrated area ( $A_G$ ) for a few specific domains, such as the 12.4° domain in Figure 1b, while all others show similar  $A_G$  ( $\sim 1.5\times$  that of SLG). We obtain full Raman spectra for each domain (see Figure 1b), allowing us to detail the quantitative relationship between G band area ( $A_G$ ), twist angle ( $\theta$ ), and laser excitation energy ( $E_{\text{ex}}$ ). Figure 2a shows a plot of  $A_G$  (normalized to  $A_G$  for SLG) vs  $\theta$ , measured at  $E_{\text{ex}} = 2.33 \text{ eV}$ .  $A_G$  follows a universal curve as a function of  $\theta$ , with peak enhancement at  $\theta_{\text{peak}} = 12.5 \pm 0.1^\circ$ . Furthermore, we find an approximately linear relationship between  $E_{\text{ex}}$  and  $\theta_{\text{peak}}$ . Figure 2b shows widefield G band images of the same BLG area at three different excitation energies. For each, a different domain exhibits enhancement, with  $\theta$  later identified with DF-TEM. Over 0.8 eV of variation in  $E_{\text{ex}}$ , we find that  $\theta_{\text{peak}}$  changes by  $\sim 6^\circ$  (Figure S1); we plot these points in Figure 2b. Combined, our data unambiguously show that the enhancement in  $A_G$  has a universal, one-to-one correspondence with  $\theta$  for CVD tBLG. While similar behavior was observed by others,<sup>21,23</sup> our data provide the first direct and spatially resolved confirmation of its structural origin.

This  $\theta$ -dependent behavior cannot be the result of the optical transitions expected within two isolated graphene sheets, which should provide uniform, broadband characteristics.<sup>1</sup> Instead, to determine its main cause, we detail below a general description of all possible optical transitions and their efficiencies in tBLG; our description also allows comparisons between different mechanisms for G band enhancement, including the “double



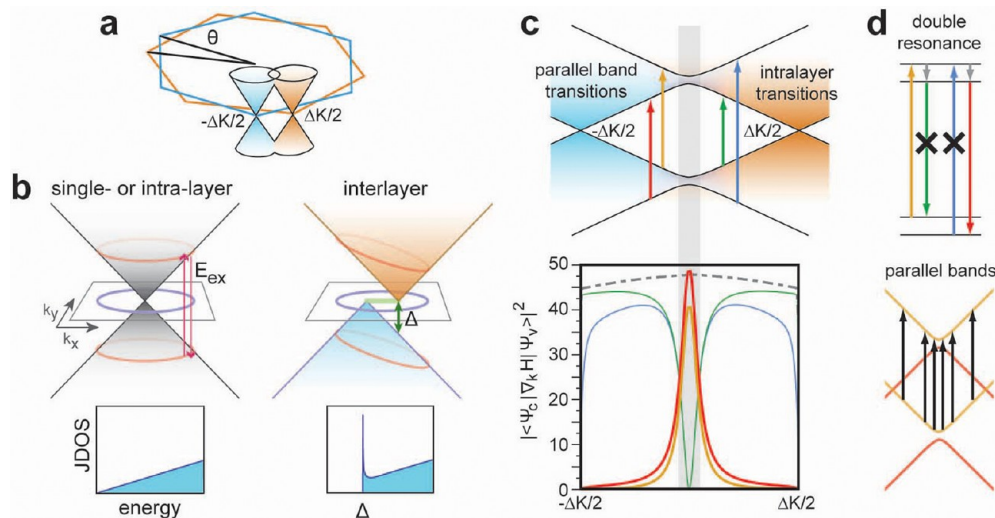


**Figure 3.** (a) Band structure of tBLG for noninteracting layers. The Dirac cones from each layer (orange, blue) are separated in  $k$  space by the twist angle  $\theta$ . (b) Schematics of the two types of optical transitions, intra- and interlayer, which conserve momentum in noninteracting tBLG. No interlayer transitions are allowed below an energy  $\Delta$ , but there is a large singularity in the interlayer JDOS at  $\Delta$  due to the parallel valence and conduction bands. (c) A slice through the band structure of tBLG with interlayer interaction, which causes splitting of the electronic states near the degeneracy point (shaded). Possible parallel band and intralayer transitions are labeled. Below is a plot of the square velocity matrix element, which is proportional to  $|M_{\text{op}}|^2$ , for each transition type (calculated from a tight binding model at  $13.2^\circ$ ). The dashed line is the square velocity matrix element for intralayer transitions in single layer graphene. (d) Schematics of two mechanisms considered for G band enhancement. For the previously proposed double resonance model (top), one optical transition in both of the possible pathways is not allowed. On the other hand, parallel band transitions have a high JDOS and are significant over many states.

resonance” model proposed previously.<sup>21</sup> We examine two key factors, the joint density of states (JDOS) and the optical transition matrix element ( $M_{\text{op}}$ ), which govern the strength of absorption and Raman scattering. We find that it is necessary to include a new class of transitions, “parallel band” optical transitions, which have not been explicitly studied before in tBLG; on the basis of our considerations of the JDOS and  $M_{\text{op}}$  of the available optical transitions in tBLG, we conclude that parallel band optical transitions are the prevailing cause of the observed G band enhancement.

First, we discuss the JDOS for optical transitions in tBLG. Initially, we consider the band structure of tBLG with a twist angle  $\theta$  for noninteracting layers, which is two sets of six Dirac cones, also separated by  $\theta$  (Figure 3a). In principle, there exist two types of transitions for every value of  $k$ : intralayer and interlayer optical transitions. The JDOS of SLG, as well as intralayer transitions in tBLG, can be derived by mapping all of the states within a pair of Dirac cones sharing the same apex ( $K$  point) that satisfy the momentum and energy conservation for a given  $E_{\text{ex}}$ . These states form a pair of circles whose diameter increases linearly with  $E_{\text{ex}}$ , resulting in the well-known linear JDOS vs energy ( $E$ ) (Figure 3b, left). We use the same selection rules to examine interlayer transitions (Figure 3b, right). From Figure 3b, it is clear that interlayer transitions are forbidden below an energy of  $\Delta = \hbar v_F(\Delta K)$ , where  $\Delta K$  is the  $k$  space separation between the apexes of the two cones. However, there are many states between  $k = \pm\Delta K/2$ , where the valence and conduction cones run parallel to each other, with a transition energy near  $\Delta$ . We can analytically derive the JDOS for this transition as a function of  $E$  (see Supporting Information), which is given by

$$(\sqrt{1 - (\Delta/E)^2} + 1/\sqrt{1 - (\Delta/E)^2})(E/\pi\hbar^2v_F^2)$$

This expression approaches the single layer JDOS for  $E \gg \Delta$ , but the second term diverges as  $E \sim \Delta$ , producing a singularity in the interlayer JDOS for tBLG.

The electronic interaction between the two layers results in two main modifications to this model. First, splitting occurs at the degeneracy points in the band structure of tBLG. Second, near the degeneracy point, optical transitions are no longer strictly interlayer or intralayer because the relevant states are hybridized from both layers. However, the bands corresponding to the original interlayer transition continue to run parallel to each other through the avoided crossing (see Figure 3c,d). We refer to the transitions between these bands as “parallel band” transitions, which captures their behavior both near and away from the degeneracy point. While the splitting leads to additional van Hove singularities in the single-particle electronic density of states, as observed with scanning tunneling spectroscopy,<sup>19</sup> it has a small effect on JDOS for both the parallel band and intralayer optical transitions (Figure S2) because the states affected by this splitting are a small subset of the total states which contribute to either type of transition.

We next consider the optical transition matrix element,  $M_{\text{op}}$ , for both parallel band and intralayer transitions. We have used a tight binding model at a commensurate angle ( $13.2^\circ$ , see Figure S3) to calculate  $M_{\text{op}}$  for these transitions in tBLG. Figure 3c shows a plot of the square velocity matrix element ( $\propto (\omega M_{\text{op}})^2$ , see Supporting Information) in  $k$ -space for all possible types of transitions. Our calculations provide two central results. First, they show that intralayer transitions are suppressed near the degeneracy point. Immediately, this suggests that the previously proposed double resonance process for G band enhancement, which utilizes intralayer and parallel band transitions simultaneously (Figure 3d), is weak near the degeneracy point and is unlikely to provide a full explanation for our data. Also, as discussed previously, the JDOS associated with this process (i.e., states where splitting occurs) is

comparatively small, which further diminishes the effect of double resonance.

Second, we find that parallel band transitions are optically active for all participating states; their strength is maximum (almost equivalent to that of SLG) near the degeneracy point and monotonically decreases away from it, with a long tail. Considering the large JDOS and  $M_{op}$  for parallel band transitions (Figure 3b, right), we expect that they should cause a measurable increase in both Raman intensity and absorption (proportional to  $\text{JDOS} \times |M_{op}|^2$ ),<sup>1</sup> both at similar excitation energies (Figure 4a). Previously,  $\theta$ -dependent

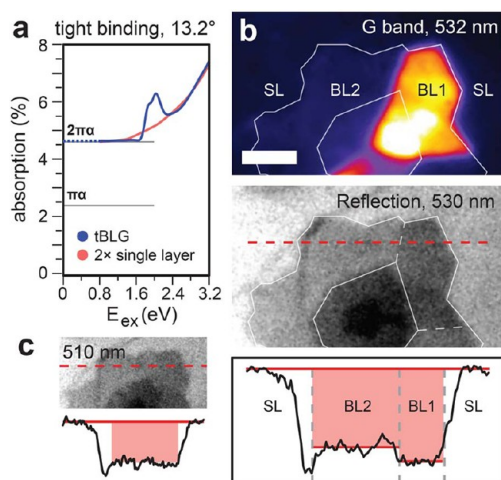


**Figure 4.** (a) Tight binding calculation of absorption in 13.2° tBLG. In comparison to two noninteracting single layer sheets, there is a peak due to parallel band transitions. (b) G band (false color) and contrast-enhanced reflection images of the same sample on Si/285 nm SiO<sub>2</sub> (scale bar 2  $\mu$ m). There is a small increase in contrast in the same region and at the same wavelength where the G band is enhanced (contrast plot is averaged over  $\sim 1 \mu$ m, linear background subtracted). (c) Image of the same region at 510 nm; the contrast disappears to within the noise limit.

variations in optical conductivity of up to  $\sim 50\%$  were found in tBLG<sup>26</sup> but were not correlated with Raman data. As we expect, for a domain that exhibits a strong G band enhancement at  $\lambda_{ex} = 532$  nm, we observe a small contrast increase on a Si/285 nm SiO<sub>2</sub> substrate (contrast is approximately proportional to absorption in this case<sup>26</sup>) at  $\lambda = 530$  nm (10 nm fwhm optical bandpass filter, see Figure 4b). At  $\lambda = 510$  nm, this contrast disappears to within the noise limit (Figure 4c).

In contrast to the small increase in the absorption signal, the G band enhancement is much stronger (Figures 4 and 1a). This substantial increase is due to quantum interference effects particular to resonance Raman scattering.<sup>31,32</sup> In general, every possible Raman pathway has a phase, which has a different polarity depending on whether the excitation energy is above or below the energy difference between the electronic states in the resonant Raman transition; for a system with many available states, these pathways can interfere constructively or destructively. In single-layer graphene, for example, many pathways interfere destructively due to the linear JDOS (Figure 3b), weakening the overall intensity.<sup>31,32</sup> Near the parallel band singularity in tBLG, on the other hand, many states with the same energy difference should add constructively, leading to a considerable G band enhancement at  $E_{ex} \sim \Delta$ . To verify the

significance of these effects, we include all possible transitions in a simplified expression for the Raman intensity (see Figure S5) in tBLG with varying  $\theta$ . Indeed, we find that parallel band transitions provide a G band enhancement near  $\theta_{peak}$  which is more than an order of magnitude larger than the absorption signal. As expected, we calculate that the double resonance process provides only a minor contribution to the G band behavior. Slight adjustment of the coupling parameters calculated with tight binding (see Supporting Information) provides us with the fit to our data shown in Figure 2a. We can also compare the values of  $E_{ex}$  vs  $\theta_{peak}$  that we determined experimentally to a plot of  $\Delta$  vs  $\theta$  (Figure 2b), which we estimate as the energy where the cones from each layer overlap in a noninteracting tight binding model. They coincide very closely, which confirms that the parallel band optical transitions alone also provide a quantitative prediction of this parameter. Despite the strong similarity between our theory and data, our current model does not consider spatial and temporal variations that exist in the structure of our tBLG samples, including changes in interlayer spacing (Figure S7), commensurability, and strain.<sup>10</sup> To account for these variations, which occur on scales less than our  $\sim 1 \mu$ m spatial resolution and  $\sim 1$  min acquisition time, an accurate theory needs to describe an average behavior and explain the optical properties of incommensurate tBLG for all possible  $\theta$ . Such theories are currently lacking and beyond the scope of our current paper.

Our data and the parallel band transition model have exciting implications for future studies of tBLG. First, even though  $M_{op}$  for parallel band transitions is strongest near the degeneracy point, there is a significant contribution from other states as well, due to the long tail in  $M_{op}$  and the large contribution of these additional states to the parallel band JDOS singularity. By calculating  $\text{JDOS} \times |M_{op}|^2$  over various parts of the tBLG band structure, we estimate that roughly 50% of the absorption peak in tBLG is due to strongly hybridized states within one fwhm of the peak in  $|M_{op}|^2$  (see Figure 3c, shaded area), while 50% is due to transitions from all the other states. These states are not well hybridized between the layers but have electron densities that are strongly localized (85% or higher) in one layer; thus, the parallel band transitions outside the shaded region in Figure 3c are very close to true interlayer transitions. These interlayer transitions could lead to interesting optical properties unique to tBLG. For instance, an applied electric field between the layers should break the interlayer symmetry, splitting the energy of interlayer transitions from the valence band of layer 1 to the conduction band of layer 2 and vice versa. This could potentially enable directionally controlled optical pumping of electrons between layers. Excitons, which were not considered in this work, can be significant in similar systems with a large JDOS due to parallel bands<sup>33</sup> and could strengthen these effects.

Second, the peak in the JDOS for parallel band transitions is a robust, geometrically determined function of  $\theta$  alone. Our data and theory suggest that  $\theta_{peak}$  of the G band enhancement should be largely insensitive to factors such as the substrate, variations in growth conditions, or small variations in strain. This allows very precise optical determination of twist angle with a tunable laser. In addition, widefield Raman imaging allows rapid, spatially resolved identification of tBLG domains with a specific  $\theta$ —for instance, we can identify the bright regions in Figure 1a as tBLG domains with  $\theta = 12.5 \pm 2.5 / -1.2^\circ$  (for  $A_G$  at least  $2\times$  larger than other BLG). As illustrated in Figure 2b,  $\theta$  can be specified with  $E_{ex}$ , enabling future studies of

optical, electrical, and mechanical properties of tBLG at specific angles on arbitrary substrates. We also note that the 2D Raman intensity also provides valuable information about  $\theta$ . As shown in Figure 1b as well as in previous work,<sup>23</sup> the 2D peak intensity, width, and position all change rapidly near  $\theta_{\text{peak}}$ , which defines a transition between high and low twist angle regimes (Figure S9). While the point Raman spectra of SLG and high angle ( $\theta > \theta_{\text{peak}}$ ) tBLG are difficult to distinguish (in part because the 2D/G ratio of high angle tBLG is similar to or larger than that of SLG, see Figure S10), high angle tBLG is easily identified with WRI (see Figure 1b) because the 2D intensity is twice that of the surrounding SLG.

Finally, while  $\theta_{\text{peak}}$  only depends on  $E_{\text{ex}}$ , the magnitude of the G band enhancement and variations in 2D behavior are sensitive to the degree of interaction between layers. Thus, Raman imaging provides us with a tool to study tBLG materials in different interaction regimes on a large scale. To demonstrate this, we examine two extreme cases: CVD-grown tBLG, which is fully in contact, and two SLG layers transferred on top of each other, which are in very loose contact and separated by debris. Figure 5a shows a schematic of our sample; the artificial

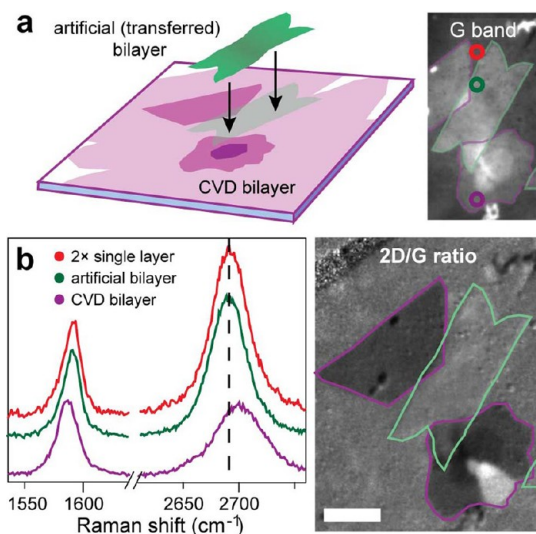


**Figure 5.** (a) Schematic of our sample and G band image showing CVD and artificial bilayer regions. (b) Raman spectra of artificial and CVD bilayer. The artificial bilayer has weak interlayer coupling, and its Raman signature is almost identically 2× nearby SLG. Consistent with the spectra, the artificial region disappears in a 2D/G ratio image (scale bar 5  $\mu\text{m}$ ).

tBLG layers are separated by 1–2 nm, as confirmed by atomic force microscopy (Figure S11). The Raman spectrum of the artificial tBLG is markedly different from that of a nearby CVD bilayer region (as grown) and is almost identically twice that of SLG (Figure 5b). Additionally, in a 2D/G ratio widefield image, the CVD bilayer graphene varies in contrast (2D/G is either higher or lower than SLG, depending on  $\theta$ ), but the entire artificial region cannot be distinguished from the 2D/G ratio of SLG, indicating that the as-is transferred layers do not interact and are completely decoupled. Annealing our artificial tBLG samples allows the layers to couple, and we see a return of the expected bilayer Raman signatures, including G band enhancement in certain regions (Figure S12).

We expect Raman spectroscopy to provide a high-throughput characterization and imaging tool for tBLG, whose mass

production is under rapid development. In particular, it enables precise, substrate-independent imaging of the twist angle. In addition, Raman imaging serves as a probe of variations in interlayer interactions, providing a unique tool for studying effects of external physical and chemical factors such as pressure, intercalation, adsorbates, and temperature on bilayer graphene and other layered materials. Furthermore, our calculations suggest that parallel band optical transitions play a key role in the optical properties of tBLG, which can be further utilized in developing novel optical or optoelectronic devices with properties highly tunable through control of twist angle.

## ■ ASSOCIATED CONTENT

### Supporting Information

Sample synthesis and characterization methods; additional G and 2D band Raman data; details of analytical, Raman, and tight binding calculations of tBLG JDOS and optical properties; AFM data on artificial tBLG. This material is available free of charge via the Internet at <http://pubs.acs.org>.

## ■ AUTHOR INFORMATION

### Corresponding Author

\*E-mail: [jpark@cornell.edu](mailto:jpark@cornell.edu).

### Notes

The authors declare no competing financial interest.

## ■ ACKNOWLEDGMENTS

The authors thank M. Wojcik, C. S. Ruiz-Vargas, and A. W. Tsen for help with sample fabrication and A. Singh for help with theoretical modeling. This work was mainly supported by the AFOSR grants (FA9550-09-1-0691, FA2386-10-1-4072) and the NSF through the Cornell Center for Materials Research (NSF DMR-1120296). This work used computational resources provided by the National Science Foundation through the Extreme Science and Engineering Discovery Environment (XSEDE) and the Texas Advanced Computing Center under Contract TG-DMR050028N. Additional funding was provided by Alfred P. Sloan Foundation. Sample fabrication was performed at the Cornell Nanoscale Science and Technology Facility, a National Nanotechnology Infrastructure Network node. R.W.H. is supported by a Graduate Research Fellowship from the National Science Foundation; L.B. was partially supported by a Fulbright scholarship.

## ■ REFERENCES

- (1) Nair, R.; Blake, P.; Grigorenko, A.; Novoselov, K.; Booth, T.; Stauber, T.; Peres, N.; Geim, A. *Science* **2008**, *320*, 1308–1308.
- (2) Malard, L.; Pimenta, M.; Dresselhaus, G.; Dresselhaus, M. *Phys. Rep.* **2009**, *473*, 51–87.
- (3) Zhang, Y.; Tang, T.; Girit, C.; Hao, Z.; Martin, M.; Zettl, A.; Crommie, M.; Shen, Y.; Wang, F. *Nature* **2009**, *459*, 820–823.
- (4) Castro, E.; Novoselov, K.; Morozov, S.; Peres, N.; Dos Santos, J.; Nilsson, J.; Guinea, F.; Geim, A.; Neto, A. *Phys. Rev. Lett.* **2007**, *99*, 216802.
- (5) Tan, P. H.; Han, W. P.; Zhao, W. J.; Wu, Z. H.; Chang, K.; Wang, H.; Wang, Y. F.; Bonini, N.; Marzari, N.; Pugno, N.; Savini, G.; Lombardo, A.; Ferrari, A. C. *Nat. Mater.* **2012**, *11*, 294–300.
- (6) Ferrari, A.; Meyer, J.; Scardaci, V.; Casiraghi, C.; Lazzeri, M.; Mauri, F.; Piscanec, S.; Jiang, D.; Novoselov, K.; Roth, S.; Geim, A. *Phys. Rev. Lett.* **2006**, *97*, 187401.
- (7) Malard, L. M.; Nilsson, J.; Elias, D. C.; Brant, J. C.; Plentz, F.; Alves, E. S.; Castro, A. H.; Pimenta, M. A. *Phys. Rev. B* **2007**, *76*, 201401.



- (8) Wang, F.; Zhang, Y. B.; Tian, C. S.; Girit, C.; Zettl, A.; Crommie, M.; Shen, Y. R. *Science* **2008**, *320*, 206–209.
- (9) Mak, K. F.; Lui, C. H.; Shan, J.; Heinz, T. F. *Phys. Rev. Lett.* **2009**, *102*, 256405.
- (10) Brown, L.; Hovden, R.; Huang, P.; Wojcik, M.; Muller, D. A.; Park, J. *Nano Lett.* **2012**, *12*, 1609–1615.
- (11) Warner, J. H.; Rummeli, M. H.; Gemming, T.; Buchner, B.; Briggs, G. A. D. *Nano Lett.* **2009**, *9*, 102–106.
- (12) dos Santos, J.; Peres, N.; Castro, A. *Phys. Rev. Lett.* **2007**, *99*, 256802.
- (13) Bistrizter, R.; MacDonald, A. *Proc. Natl. Acad. Sci. U. S. A.* **2011**, *108*, 12233–12237.
- (14) de Laissardiere, G.; Mayou, D.; Magaud, L. *Nano Lett.* **2010**, *10*, 804–808.
- (15) Mele, E. *Phys. Rev. B* **2010**, *81*, 161405.
- (16) Lui, C. H.; Li, Z. Q.; Chen, Z. Y.; Klimov, P. V.; Brus, L. E.; Heinz, T. F. *Nano Lett.* **2011**, *11*, 164–169.
- (17) Lui, C. H.; Li, Z. Q.; Mak, K. F.; Cappelluti, E.; Heinz, T. F. *Nat. Phys.* **2011**, *7*, 944–947.
- (18) Reina, A.; Jia, X.; Ho, J.; Nezich, D.; Son, H.; Bulovic, V.; Dresselhaus, M.; Kong, J. *Nano Lett.* **2009**, *9*, 30–35.
- (19) Li, G.; Luican, A.; dos Santos, J.; Neto, A.; Reina, A.; Kong, J.; Andrei, E. *Nat. Phys.* **2010**, *6*, 109–113.
- (20) Luican, A.; Li, G.; Reina, A.; Kong, J.; Nair, R.; Novoselov, K.; Geim, A.; Andrei, E. *Phys. Rev. Lett.* **2011**, *106*, 126802.
- (21) Ni, Z.; Liu, L.; Wang, Y.; Zheng, Z.; Li, L.; Yu, T.; Shen, Z. *Phys. Rev. B* **2009**, *80*, 125404.
- (22) Ni, Z.; Wang, Y.; Yu, T.; You, Y.; Shen, Z. *Phys. Rev. B* **2008**, *77*, 235403.
- (23) Kim, K.; Coh, S.; Tan, L. Z.; Regan, W.; Yuk, J. M.; Chatterjee, E.; Crommie, M. F.; Cohen, M. L.; Louie, S. G.; Zettl, A. *arXiv:1201.4221v2*, 2012.
- (24) Poncharal, P.; Ayari, A.; Michel, T.; Sauvajol, J. L. *Phys. Rev. B* **2008**, *78*, 113407.
- (25) Carozo, V.; Almeida, C.; Ferreira, E.; Cancado, L.; Achete, C.; Jorio, A. *Nano Lett.* **2011**, *11*, 4527–4534.
- (26) Wang, Y.; Ni, Z.; Liu, L.; Liu, Y.; Cong, C.; Yu, T.; Wang, X.; Shen, D.; Shen, Z. *ACS Nano* **2010**, *4*, 4074–4080.
- (27) Blake, P.; Hill, E.; Neto, A.; Novoselov, K.; Jiang, D.; Yang, R.; Booth, T.; Geim, A. *Appl. Phys. Lett.* **2007**, *91*, 063124.
- (28) Havener, R. W.; Ju, S.-Y.; Brown, L.; Wang, Z.; Wojcik, M.; Ruiz-Vargas, C. S.; Park, J. *ACS Nano* **2012**, *6*, 373–380.
- (29) Huang, P.; Ruiz-Vargas, C.; van der Zande, A.; Whitney, W.; Levendorf, M.; Kevek, J.; Garg, S.; Alden, J.; Hustedt, C.; Zhu, Y.; Park, J.; McEuen, P.; Muller, D. *Nature* **2011**, *469*, 389–392.
- (30) Kim, K.; Lee, Z.; Regan, W.; Kisielowski, C.; Crommie, M.; Zettl, A. *ACS Nano* **2011**, *5*, 2142–2146.
- (31) Chen, C.; Park, C.; Boudouris, B.; Horng, J.; Geng, B.; Girit, C.; Zettl, A.; Crommie, M.; Segalman, R.; Louie, S.; Wang, F. *Nature* **2011**, *471*, 617–620.
- (32) Basko, D. *New J. Phys.* **2009**, *11*, 095011.
- (33) Yang, L. *Phys. Rev. B* **2011**, *83*, 085405.